Real-Space Observation of Skyrmionium in a Ferromagnet-Magnetic Topological Insulator Heterostructure

Shilei Zhang,[†] Florian Kronast,[‡] Gerrit van der Laan,[¶] and Thorsten Hesjedal[*,†]

†*Clarendon Laboratory, Department of Physics, University of Oxford, Parks Road, Oxford, OX1 3PU, United Kingdom*

‡*Helmholtz-Zentrum Berlin für Materialien und Energie, Albert-Einstein-Strasse 15, 12489 Berlin, Germany*

¶*Magnetic Spectroscopy Group, Diamond Light Source, Didcot, OX11 0DE, United Kingdom*

E-mail: Thorsten.Hesjedal@physics.ox.ac.uk;Telephone:+44-1865-272235

Abstract

The combination of topological insulators, i.e., bulk insulators with gapless, topologically protected surface states, with magnetic order is a love-hate relationship that can unlock new quantum states and exotic physical phenomena, such as the quantum anomalous Hall effect and axion electrodynamics. Moreover, the unusual coupling between topological insulators and ferromagnets can also result in the formation of topological spin textures in the ferromagnetic layer. Skyrmions are topologically-protected magnetization swirls that are promising candidates for spintronics memory carriers. Here, we report on the observation of skyrmionium in thin ferromagnetic films coupled to a magnetic topological insulator. The occurrence of skyrmionium, which appears as a soliton composed of two skyrmions with opposite winding numbers, is tied to the ferromagnetic state of the topological insulator. Our work presents a new combination of two important classes of topological materials and may open the door to new topologically inspired information-storage concepts in the future.

Keywords: Skyrmionium; topological insulator; magnetic imaging; spintronics; topological quantum matter

Dissipationless currents in topological insulators (TIs) have been an area of intense research in the past years.[1–3] TIs are bulk insulators, but with gapless surface or edge states. The topological surface state (TSS) in three-dimensional (3D) TIs is characterized by spin-momentum locking, whereby counter-propagating states always appear in pairs.[2,3] Magnetic doping of the TI, on the other hand, can lift this degeneracy and split the spin-polarized bands.[3,4] In particular, out-of-plane magnetic moments can open a mass gap in the TSS and lead to quantized Hall conductance if the Fermi energy is tuned to reside in this mass gap.[5] This quantum anomalous Hall (QAH) state has been theoretically predicted[5–10] and experimentally confirmed in Cr- and V-doped $(Sb,Bi)_2(Se,Te)_3$,[11–17] and it is a prerequisite for unlocking a plethora of quantum phenomena,[2,14,18,19] also paving the way for future applications.[20,21]

An alternative way of introducing a magnetic gap in the Dirac states,[4] or to raise the

transition temperature of a magnetic TI,[22,23] is by means of proximity-coupling to a ferro- or ferrimagnetic thin film.[24–26] Ideally, the magnetic exchange coupling is via the Dirac electrons, in turn leading to gapless chiral edge states in the TI. When the magnetic material is not homogeneous, e.g., if it is patterned or contains domains, a one-dimensional, gapless chiral edge state can appear at the discontinuity.[12,27]

Magnetic skyrmions, on the other hand, are topologically stable, swirl-like magnetization configurations.[28–31] Skyrmions are proposed as next-generation information carriers that allow for high-density storage, logic operation, and low-energy consumption,[32,33] given their topological protection which prevents their unwinding, as compared to, e.g., ordinary magnetization vortex patterns, and the ease of manipulation as compared to magnetic domain walls.[29–31] In chiral bulk magnets, where the Dzyaloshinskii-Moriya interaction (DMI) results from the broken inversion symmetry, the formation of skyrmion is governed by a hierarchy of energy scales, reaching from strong exchange interactions, spin-orbit coupling, to crystal field terms.[34] Moreover, the naturally broken inversion symmetry at the surface allows for a superexchange interaction to take place via spin-orbit coupling, leading to a DMI term as well.[33,35–37] In surface DMI systems, such as Pt/Co/AlO_x/Pt, nanoscale bubble skyrmions have been observed at room temperature.[33,38,39] In magnetism, the topology of spin order manifests itself in the topological winding number (N) which plays a pivotal role for the determination of the emergent properties of a system.[32] N is an integer that counts the number of times the physical space fully covers the order parameter space, and it can be experimentally determined by resonant x-ray scattering.[40] Skyrmions in bulk DMI systems typically have a winding number of $N = 1$, whereas e.g. $La_{2-2x}Sr_{1+2x}Mn_2O_7$ carries $N = 2$ skyrmions.[41] Another type of skyrmion are $N = 0$ systems with a double-twisted core, so-called skyrmionium, 2π vortex,[42,43] or target skyrmion,[44] has been been theoretically proposed and experimentally verified,[45–47] most recently in the frustrated kagome magnet Fe_3Sn_2[48] and a patterned FeGe nanodisk.[49] Moreover, isolated skyrmionium has been nucleated by optical means,[43] and its motion can be controlled by magnetic field gradients[47]

and spin-polarized currents,[50] opening the door for their application in spintronics devices.

Here, we report the observation of skyrmionium in a ferromagnetic layer, proximity-coupled to a magnetically doped TI. Using x-ray photoemission electron microscopy (XPEEM), we are able to unambiguously identify the topologically non-trivial skyrmion state in the ferromagnetic top layer, while the magnetically doped TI is below its transition temperature T_C and long-range ordered. Once heated above the magnetic ordering temperature of the magnetic TI, the skyrmionium spin texture disappears. This shows that magnetic configurations of distinct topology can be imprinted in a ferromagnetic layer, depending on the TSS-mediated exchange coupling strength with respect to the ferromagnetic layer thickness. We discuss this observation in the context of gapped chiral edge states, which seem to mediate the additional exchange interaction, giving rise to the non-collinear magnetic patterns.

XPEEM is a powerful tool for the element-selective imaging of magnetic domains with a lateral resolution of 10's of nm (see Methods).[51,52] The magnetic contrast is provided by x-ray magnetic circular dichroism (XMCD) that detects the difference in x-ray absorption depending on the relative orientation between incident x-ray helicity vector $\mathbf{P}$ and magnetization, i.e., $\mathbf{M}$ by $I_{\mathrm{XMCD}} = \mathbf{P} \cdot \mathbf{M}$. Compared to other magnetic imaging techniques, XPEEM produces a signal that is directly proportional to the projection of the local spin moments onto the x-ray helicity vector.[53] For our experiments, we chose an incident angle of the x-rays of 16°, making XPEEM sensitive to all three magnetization components and thus ideally suited for studying complex spin textures.[54]

The measured XPEEM contrast (Figure 1) shows the same magnetization direction in the center of the ring as in the surrounding matrix, and a reversed magnetization in a ring around the center. This magnetization pattern can be obtained by nesting two skyrmions with opposite winding number, i.e., $N = \pm 1$, leading to a composite object with winding number 0 (Figure 2a-d). By changing the azimuthal direction of the incident x-rays with respect to the magnetic object by 90°, it is possible to determine the symmetry of the magnetization pattern.[54] While the basic shape of the contrast is the same for the x-rays

coming in from the left (Figure 1a) and from the top (Figure 1b), the dark red feature rotates with the beam, consistent with a rotationally invariant magnetization pattern.

Due to the existence of the DMI, there are essentially two different types of individual skyrmions that can be classified depending on the character of the domain wall delimiting the central domain: Bloch skyrmions and Néel skyrmions. The former are often referred to as chiral skyrmions. Both have a S^2 winding number ("skyrmion number") $N = \pm 1$ (cf. ref.[55]).

A skyrmionium, as a composite particle, is derived from these basic skyrmion structures (cf. Figure 2). While the total S^2 winding number of this composite object is zero, the cross-sectional cuts through the center of the magnetization pattern consist of two subsequent 2π domain walls of Bloch or Néel character with a net rotation sense and thus a nonzero S^1 winding number ± 2 (cf. ref.[56]). For this reason we may distinguish the following structures shown in Figure 2: (a) diverging Néel-type (diverging at its center), (b) converging Néel-type, (c) left-chiral Bloch-type (rotation sense with respect to its center), and (d) right-chiral Bloch-type. The cross-sectional cuts through the center of the magnetization patterns are shown below. Néel-type walls show a cycloidal continuous rotation of magnetic moments within a plane normal to the domain wall. For instance, a "left-handed" cycloidal spin spiral has a structure $\downarrow\searrow\rightarrow\nearrow\uparrow\nwarrow\leftarrow\swarrow\downarrow$ as one proceeds from left to right, which corresponds with a converging Néel type skyrmion. In this notation, the diverging Néel-type can therefore also be called "right-handed". Note that the nonzero S^1 winding number of this cut is not at variance with the topological triviality of the skyrmionium as the magnetization can vary on S^2 as is evident if one considers a series of cuts that are parallel to a cut through the center of the skyrmionium. This fact is reflected by the triviality of the homotopy group $\pi_1(S^2) = 0$.[55]

The corresponding simulated XPEEM contrast images are shown further below in Figure 2, which were obtained for the x-rays coming from the left (middle row, f-i) and from above (bottom row, k-n), using $\mathbf{M}$ by $I_{\mathrm{XMCD}} = \mathbf{P} \cdot \mathbf{M}$. Note that a conventional skyrmion and

skyrmionium have fundamentally different XPEEM contrast, as shown for a diverging Néel-type skyrmion in Figure 2e,j,o. Comparing these calculated contrast patterns with the experimental data shown in Figure 1, we can conclude that the observed magnetization texture is diverging Néel-type skyrmionium, rather than a single skyrmion.

The magnetic TI films, Cr-doped Sb_2Te_3, were grown by molecular beam epitaxy (MBE) on *c*-plane sapphire substrates, as described in the Methods section and Ref.[57,58] Cr-doped $(Sb,Bi)_2Te_3$ has been the key material for observing the QAH effect.[11,16] In these films the Landau level spectrum is easily observable, even at higher Cr doping levels,[12,15,59] and the magnetic ordering temperature can be above 100 K without loss of crystalline quality.[60] Subsequent to loading the samples into the ultra-high vacuum chamber of the XPEEM system, the Cr-doped Sb_2Te_3 samples were sputter-cleaned. X-ray absorption spectroscopy (XAS) was carried out at the $L_{2,3}$ edges of Cr at a temperature of 70 K (Figure 3c). The XAS lineshape is indicative of nominal Cr^{2+}, consistent with substitutional Cr doping on Sb sites[57,61] Next, a ferromagnetic top layer with a low magnetocrystalline anisotropy, $Ni_{80}Fe_{20}$ (NiFe, for short), was deposited *in-situ* using an electron beam evaporator. By using a knife-edge, a 20-μm-wide wedge was deposited (layer thickness ranging from 0 to 3 nm). Wedge-shaped films are an easy way to study the effects of the ferromagnetic layer thickness on the magnetic coupling scenario.

By tuning the energy of the incident x-rays to the $L_{2,3}$ edges of Fe and Cr, respectively, the magnetization patterns in both the ferromagnetic top layer and the magnetic TI layer can be determined independently. This unique ability is crucial in order to separate the trivial effects of dipolar coupling, or other direct proximity effects, from additional, TI-related mechanisms. Figure 2a shows a distribution of mostly oppositely magnetized domains in the magnetic TI film (at 70 K, i.e., below T_C), measuring several 100 nm in size. By varying the temperature, and judging from the disappearance of the Cr-XPEEM domain pattern in the Cr:Sb_2Te_3 film at 100 K (Figure 3b), a magnetic transition temperature of $\sim$100 K was determined above which it shows no magnetic long-range order.

Next, we investigated the temperature-dependence of the magnetic contrast in the ferromagnetic top layer by recording XPEEM images at the Fe edge. Figure 4 shows overview images obtained at different temperatures (increasing from top to bottom) across the NiFe wedge. At all temperatures, above the edge, no contrast is found (the edge is almost horizontal). With increasing NiFe film thickness (towards the bottom of the image), larger magnetic features appear at 60 K. With increasing temperature (80 K), but still below the T_C of the magnetic TI film, ring-like features can be observed in the lower half of the image. Once the temperature is increased above the T_C of Cr:Sb_2Te_3, the magnetic contrast in the top layer almost completely disappears (lower image, obtained at 120 K). By comparing the magnetic domain pattern observed in the ferromagnetic top layer (Figure 1a and Figure 4, top) with that of the magnetic TI (Figure 3a), it can be concluded that both patterns are not directly correlated. Nevertheless, the magnetic contrast in the NiFe layer is directly dependent on the magnetic state of the underlying magnetic TI film.

Next, the magnetic contrast was studied as a function of applied field. Using a special sample holder, magnetic fields of up to 50 mT were applied perpendicular to the sample surface.[62] The XPEEM measurements were then carried out at the Fe edge in the applied field as indicated. Figure 5 shows the field dependence of the magnetization in the NiFe film at a temperature of 40 K (field increasing from top to bottom). The edge of the NiFe wedge is roughly horizontal (at the very top of the images). At a low applied field, the region close to the edge shows a number of magnetic features that extend into the thicker areas of the film (the wedge thickness ranges from 0 to 3 nm). The crescent-shaped feature in the bottom-right corner starts to separate off from the edge, forming isolated skyrmionium, as the field is increased to 4 mT. Further, another ring starts to form as the field is increased to 4.4 mT. At 8.8 mT, this second ring starts to decompose, while the dominant skyrmionium ring structure gets stronger in contrast. It also moves further away from the edge and reduces in diameter. Above 11 mT, the diameter increases again, until above 13.2 mT, the skyrmionium structure fully disappears. No signs of a skyrmion pair are found, which is a possible decay

process for unzipping $N = 0$ skyrmionium into a skyrmion pair with $N = \pm 1$.[46] Instead, a possible decay scenario could be analogous to 2π domain walls via decay through the 3rd dimension.[56]

The investigation of a wedge-shaped ferromagnetic film, proximity-coupled to a magnetic TI, has the unique advantage of probing the different coupling regimes in a single experiment. If the NiFe film is very thin, it is not ferromagnetically ordered and no contrast is observed in XPEEM. As the thickness increases, proximity coupling dominates the behavior of the film, until above a certain thickness, the demagnetization energy starts to dominate. This behavior suggests the presence of an interfacial coupling term that is unique to the underlying TI.

However, if the coupling would be directly linked to the TSS, it should only be weakly temperature dependent.[63] In contrast, we found that the occurrence of skyrmionium is directly linked to the T_C of the long-range magnetically ordered state of the TI. Note that neither the magnetic TI above its transition temperature, nor an undoped TI thin film substrate (Sb_2Te_3 film on c-plane sapphire), leads to the observed non-trivial magnetization pattern. Whereas in the undoped case of a 'normal' TI (quantum spin Hall (QSH) state), the gapless TSS is characterized by counter-propagating, spin-momentum locked electrons, below T_C in a magnetically doped TI, the exchange coupling between the Dirac electrons and the magnetic impurities opens up a gap in the TSS spectrum.[6,12] This gives rise to spin-polarized channels (QAH state) (Figure 6, right hand side). This exchange coupling mechanism could also be the origin of the additional interfacial coupling term in our case, however now coupling the moments in the ferromagnetic top layer (Figure 6), which breaks down as the TSS becomes gapless above T_C. Note that the observation of the QAH effect in transport experiments is restricted to temperatures below 1-2 K in our materials,[13,14,25] however, a magnetic gap should nevertheless exist up to T_C.

Another aspect worth considering is the effect that the spatially nonuniform magnetization distribution in NiFe layer has on the TI, which can lead to emerging phenomena.[64,65]

For example, a magnetic domain wall in proximity to the Dirac electrons generates a chiral edge state, which in turn alters its dynamics and stability,[27,64,66–69] and vice versa. In skyrmions, this can lead to confinement of Dirac states at circular positions where the out-of-plane magnetization vanishes, further leading to charging.[70] In skyrmionium this could lead to two rings carrying dissipationless edge currents around the center of the structure.

Recently, it was suggested that the persistent currents carried by the Dirac electrons in TI-ferromagnet structures have a similar effect on the magnetization dynamics as an intrinsic DMI interaction in B20-type helimagnets.[67,68] The values of the effective DMI constant D favoring skyrmionium (or larger skyrmions) have to be large enough to suppress the simple ferromagnetic state, yet smaller than the values leading to higher order skyrmions.[46] In simulations of skyrmion formation in a confined geometry (nanodisk), a value of $D > 4\ \mathrm{mJ\,m^{-2}}$ was given.[46] It can be expected that the effective D for our system is very small given the large diameter of skyrmionium on the μm scale.

Finally, note that the strong spin-transfer torque effects which were observed in the context of magnetization switching in NiFe/Bi_2Se_3 bilayers[20] do not play a role in our case as no magnetic domains are observed in the NiFe films when the magnetic TI film is above T_C, nor in case of NiFe/Sb_2Te_3.

In summary, we presented experimental evidence for the formation of topologically non-trivial magnetization patterns on the surface of a ferromagnetic layer, coupled to a magnetic TI below its ordering temperature. The formation of skyrmionium, a soliton composed of two skyrmions with opposite topological numbers, is intimately linked to the occurrence of magnetic order in the TI, and thus a fully spin-polarized TSS. Passing through the magnetic phase transition suppresses this magnetic coupling scenario, consequently removing the additional surface DMI. In our work, we presented the interplay between two of the most intriguing topologically ordered solid state systems, thereby inspiring future work into engineered surface interactions. The combination of magnetic layers and TIs opens the door to topological spintronics, and potentially enables novel quantum computing devices, e.g., the

design of magnetically confined quantum bits,[71] which are isolated from surrounding TSSs and further topologically protected.

Sample preparation. The Cr-doped Sb_2Te_3 magnetic TI thin film samples were grown by molecular beam epitaxy (MBE) on *c*-plane sapphire substrates from elemental sources. A typical flux ratio of Te:(Cr+Sb) of 10:1 was maintained to suppress Te antisite defects. Our established two-step growth recipe was used, starting with an undoped, ∼5-nm-thick Sb_2Te_3 nucleation layer at a substrate temperature of ($T_{\mathrm{sub}} = 200$ °C), followed by an annealing step and further overgrowth of the doped film at 250 °C). For more details see Ref.[57,58] After transferring the samples to the x-ray photoemission electron microscope (XPEEM) system, they were carefully sputter cleaned at $p = 1.2 \times 10^{-5}$ mbar for 10 min each at 1.1 keV, 800 eV, and finally 400 eV ($I = 20$ μA), respectively. After x-ray spectroscopic analysis (see Fig. 3), a permalloy ($Ni_{81}Fe_{19}$) wedge was deposited *in-situ*, allowing for a fast screening of thickness-dependent coupling effects.

Element-specific magnetic characterization. X-ray absorption spectroscopy (XAS) and magnetic circular dichroism (XMCD)[72,73] were carried out in the XPEEM system[51] at beamline UE49-PGM1 (BESSY II, Berlin, Germany).[74] XPEEM is capable of spatially resolving the magnetization of a sample surface element-selectively with a resolution down to 30 nm over a 5-μm-wide field-of-view.[52] The magnetic contrast in XPEEM is relying on XMCD, which is the difference between the XAS signals obtained with oppositely circularly polarized soft x-rays, tuned to the absorption edge of an element of interest. In XPEEM, the photoelectrons ejected from the surface[75] pass through a series of lenses to obtain a magnified image of the relative orientation of the local magnetization with respect to the incoming x-ray beam,[73] enhanced by using oppositely circularly polarized light. For investigating the Fe and Cr $L_{2,3}$ edges, the x-ray energy was tuned to 700-730 eV and 570-600 eV, respectively. The sample normal was tilted 16° away from the direction of the incident x-ray beam, making XPEEM sensitive to all three components of the magnetization vector, whereby the sensitivity towards in-plane components is three times that of the our-of-plane component.[54] Unlike other magnetic imaging techniques, such as electron holography, Lorentz transmission

electron microscopy, and magnetic force microscopy, XPEEM produces a signal that is directly proportional to the local magnetic moment of the sample, rather than to the magnetic induction or external stray field created by the sample.[53] Consequently, the application of inverse recovery methods, which do not give unambiguous information about the magnetization pattern, can be avoided. Using a special sample holder, magnetic fields of up to 50 mT were applied perpendicular to the sample surface while maintaining temperature control at low temperatures.[62] Unless otherwise stated, the magnetic state was imaged at remanence.

Acknowledgement

This publication arises from research funded by the John Fell Oxford University Press Research Fund and EPSRC (EP/N032128/1). We acknowledge the Helmholtz-Zentrum Berlin for provision of synchrotron radiation beamtime at beamline UE49 of BESSY II under proposal number 15102147. The research leading to these results has received funding from the European Community's Seventh Framework Programme (FP7/2007-2013) under grant agreement no. 312284. We thank Alex A. Baker and Dr. Sergio Valencia Molina for help with the initial XPEEM experiments.

Author Contributions

The experiment was conceived by T.H. and G.v.d.L. and it was performed by all authors. All authors contributed to the discussion of the results, and S.L.Z. and T.H. wrote the manuscript with input and comments from all authors.

Notes

The authors declare no competing financial interest.

References

(1) Kane, C.; Mele, E. *Phys. Rev. Lett.* **2005**, *95*, 146802.

(2) Hasan, M. Z.; Kane, C. L. *Rev. Mod. Phys.* **2010**, *82*, 3045–3067.

(3) Qi, X.-L.; Zhang, S.-C. *Rev. Mod. Phys.* **2011**, *83*, 1057–1110.

(4) Chen, Y. L. et al. *Science* **2010**, *329*, 659–662.

(5) Qi, X.-L.; Hughes, T. L.; Zhang, S.-C. *Phys. Rev. B* **2008**, *78*, 195424.

(6) Haldane, F. D. M. *Phys. Rev. Lett.* **1988**, *61*, 2015–2018.

(7) Onoda, M.; Nagaosa, N. *Phys. Rev. Lett.* **2003**, *90*, 206601.

(8) Qi, X.-L.; Wu, Y.-S.; Zhang, S.-C. *Phys. Rev. B* **2006**, *74*, 085308.

(9) Liu, C. X.; Qi, X. L.; Dai, X.; Fang, Z.; Zhang, S. C. *Phys. Rev. Lett.* **2008**, *101*, 146802.

(10) Yu, R.; Zhang, W.; Zhang, H.-J.; Zhang, S.-C.; Dai, X.; Fang, Z. *Science* **2010**, *329*, 61–64.

(11) Chang, C.-Z. et al. *Science* **2013**, *340*, 167–170.

(12) Checkelsky, J. G.; Yoshimi, R.; Tsukazaki, A.; Takahashi, K. S.; Kozuka, Y.; Falson, J.; Kawasaki, M.; Tokura, Y. *Nat. Phys.* **2014**, *10*, 731–736.

(13) Kou, X.; Guo, S.-T.; Fan, Y.; Pan, L.; Lang, M.; Jiang, Y.; Shao, Q.; Nie, T.; Murata, K.; Tang, J.; Wang, Y.; He, L.; Lee, T.-K.; Lee, W.-L.; Wang, K. L. *Phys. Rev. Lett.* **2014**, *113*, 137201.

(14) Kandala, A.; Richardella, A.; Kempinger, S.; Liu, C.-X.; Samarth, N. *Nat. Commun.* **2015**, *6*, 7434.

(15) Bestwick, A. J.; Fox, E. J.; Kou, X.; Pan, L.; Wang, K. L.; Goldhaber-Gordon, D. *Phys. Rev. Lett.* **2015**, *114*, 187201.

(16) Chang, C.-Z.; Zhao, W.; Kim, D. Y.; Zhang, H.; Assaf, B. A.; Heiman, D.; Zhang, S.-C.; Liu, C.; Chan, M. H. W.; Moodera, J. S. *Nat. Mater.* **2015**, *14*, 473–477.

(17) Grauer, S.; Schreyeck, S.; Winnerlein, M.; Brunner, K.; Gould, C.; Molenkamp, L. W. *Phys. Rev. B* **2015**, *92*, 201304.

(18) Tse, W.-K.; MacDonald, A. H. *Phys. Rev. Lett.* **2010**, *105*, 057401.

(19) Wang, J.; Lian, B.; Zhang, S.-C. *Phys. Rev. Lett.* **2015**, *115*, 036805.

(20) Mellnik, A. R.; Lee, J. S.; Richardella, A.; Grab, J. L.; Mintun, P. J.; Fischer, M. H.; Vaezi, A.; Manchon, A.; Kim, E. A.; Samarth, N.; Ralph, D. C. *Nature* **2014**, *511*, 449–451.

(21) Zhang, X.; Zhang, S.-C. *Proc. SPIE* **2012**, *8373*, 837309.

(22) Vobornik, I.; Manju, U.; J., F.; Borgatti, F.; Torelli, P.; Krizmancic, D.; Hor, Y. S.; Cava, R. J.; Panaccione, G. *Nano Lett.* **2011**, *11*, 4079–4082.

(23) Baker, A. A.; Figueroa, A. I.; Kummer, K.; Collins-McIntyre, L. J.; Hesjedal, T.; van der Laan, G. *Phys. Rev. B* **2015**, *92*, 094420.

(24) Wei, P.; Katmis, F.; Assaf, B. A.; Steinberg, H.; Jarillo-Herrero, P.; Heiman, D.; Moodera, J. S. *Phys. Rev. Lett.* **2013**, *110*, 186807.

(25) Lee, C.; Katmis, F.; Jarillo-Herrero, P.; Moodera, J. S.; Gedik, N. *Nat. Commun.* **2016**, *7*, 12014.

(26) Hirahara, T. et al. *Nano Lett.* **2017**, *17*, 3493–3500.

(27) Wakatsuki, R.; Ezawa, M.; Nagaosa, N. *Sci. Rep.* **2015**, *5*, 13638.

(28) Rößler, U. K.; Bogdanov, A. N.; Pfleiderer, C. *Nature* **2006**, *442*, 797–801.

(29) Jonietz, F.; Mühlbauer, S.; Pfleiderer, C.; Neubauer, A.; Münzer, W.; Bauer, A.; Adams, T.; Georgii, R.; Böni, P.; Duine, R. A.; Everschor, K.; Garst, M.; Rosch, A. *Science* **2010**, *330*, 1648–1651.

(30) Romming, N.; Hanneken, C.; Menzel, M.; Bickel, J. E.; Wolter, B.; von Bergmann, K.; Kubetzka, A.; Wiesendanger, R. *Science* **2013**, *341*, 636–639.

(31) Mochizuki, M.; Yu, X. Z.; Seki, S.; Kanazawa, N.; Koshibae, W.; Zang, J.; Mostovoy, M.; Tokura, Y.; Nagaosa, N. *Nat. Mater.* **2014**, *13*, 241–246.

(32) Nagaosa, N.; Tokura, Y. *Nat. Nanotechnol.* **2013**, *8*, 899–911.

(33) Fert, A.; Cros, V.; Sampaio, J. *Nat. Nanotechnol.* **2013**, *8*, 152–156.

(34) Mühlbauer, S.; Binz, B.; Jonietz, F.; Pfleiderer, C.; Rosch, A.; Neubauer, A.; Georgii, R.; Böni, P. *Science* **2009**, *323*, 915–919.

(35) Crépieux, A.; Lacroix, C. *J. Magn. Magn. Mater.* **1998**, *182*, 341–349.

(36) Bode, M.; Heide, M.; von Bergmann, K.; Ferriani, P.; Heinze, S.; Bihlmayer, G.; Kubetzka, A.; Pietzsch, O.; Blugel, S.; Wiesendanger, R. *Nature* **2007**, *447*, 190–193.

(37) Sampaio, J.; Cros, V.; Rohart, S.; Thiaville, A.; Fert, A. *Nat. Nanotechnol.* **2013**, *8*, 839–844.

(38) Belmeguenai, M.; Adam, J.-P.; Roussigné, Y.; Eimer, S.; Devolder, T.; Kim, J.-V.; Cherif, S. M.; Stashkevich, A.; Thiaville, A. *Phys. Rev. B* **2015**, *91*, 180405.

(39) Woo, S. et al. *Nat. Mater.* **2016**, *15*, 501–506.

(40) Zhang, S. L.; van der Laan, G.; Hesjedal, T. *Nat. Commun.* **2017**, *8*, 14619.

(41) Yu, X. Z.; Tokunaga, Y.; Kaneko, Y.; Zhang, W. Z.; Kimoto, K.; Matsui, Y.; Taguchi, Y.; Tokura, Y. *Nat. Commun.* **2014**, *5*, 3198.

(42) Bogdanov, A.; Hubert, A. *Phys. Stat. Sol. (b)* **1994**, *186*, 527–543.

(43) Fujita, H.; Sato, M. *Phys. Rev. B* **2017**, *95*, 054421.

(44) Leonov, A. O.; Rößler, U. K.; Mostovoy, M. *EPJ Web Conf.* **2014**, *75*, 05002.

(45) Bogdanov, A.; Hubert, A. *J. Magn. Magn. Mater.* **1999**, *195*, 182–192.

(46) Zhang, X.; Xia, J.; Zhou, Y.; Wang, D.; Liu, X.; Zhao, W.; Ezawa, M. *Phys. Rev. B* **2016**, *94*, 094420.

(47) Komineas, S.; Papanicolaou, N. *Phys. Rev. B* **2015**, *92*, 064412.

(48) Hou, Z.; Ren, W.; Ding, B.; Xu, G.; Wang, Y.; Yang, B.; Zhang, Q.; Zhang, Y.; Liu, E.; Xu, F.; Wang, W.; Wu, G.; Zhang, X.; Shen, B.; Zhang, Z. *Adv. Mater.* **2017**, *29*, 1701144.

(49) Zheng, F.; Li, H.; Wang, S.; Song, D.; Jin, C.; Wei, W.; Kovács, A.; Zang, J.; Tian, M.; Zhang, Y.; Du, H.; Dunin-Borkowski, R. E. *Phys. Rev. Lett.* **2017**, *119*, 197205.

(50) Komineas, S.; Papanicolaou, N. *Phys. Rev. B* **2015**, *92*, 174405.

(51) Stöhr, J.; Padmore, H.; Anders, S.; Stammler, T.; Scheinfein, M. *Surf. Rev. Lett.* **1998**, *5*, 1297–1308.

(52) Helmholtz-Zentrum Berlin für Materialien und Energie, *Journal of large-scale research facilities - JLSRF* **2016**, *2*, A90.

(53) Schneider, C. M.; Schönhense, G. *Rep. Prog. Phys.* **2002**, *65*, 1785–1839.

(54) Boulle, O. et al. *Nat. Nanotechnol.* **2016**, *11*, 449.

(55) Braun, H.-B. *Adv. Phys.* **2012**, *61*, 1–116.

(56) Braun, H.-B. *Phys. Rev. B* **1994**, *50*, 16485–16500.

(57) Collins-McIntyre, L. J.; Duffy, L. B.; Singh, A.; Steinke, N.-J.; Kinane, C. J.; Charlton, T. R.; Pushp, A.; Kellock, A. J.; Parkin, S. S. P.; Holmes, S. N.; Barnes, C. H. W.; van der Laan, G.; Langridge, S.; Hesjedal, T. *EPL* **2016**, *115*, 27006.

(58) Duffy, L. B.; Figueroa, A. I.; Gładczuk, L.; Steinke, N.-J.; Kummer, K.; van der Laan, G.; Hesjedal, T. *Phys. Rev. B* **2017**, *95*, 224422.

(59) Jiang, Y.; Song, C.; Li, Z.; Chen, M.; Greene, R. L.; He, K.; Wang, L.; Chen, X.; Ma, X.; Xue, Q.-K. *Phys. Rev. B* **2015**, *92*, 195418.

(60) Zhou, Z.; Chien, Y.-J.; Uher, C. *Phys. Rev. B* **2006**, *74*, 224418.

(61) Figueroa, A. I.; van der Laan, G.; Collins-McIntyre, L. J.; Cibin, G.; Dent, A. J.; Hesjedal, T. *J. Phys. Chem. C* **2015**, *119*, 17344–17351.

(62) Gierster, L.; Pape, L.; Ünal, A. A.; Kronast, F. *Rev. Sci. Instrum.* **2015**, *86*, 023702.

(63) Pan, Z.-H.; Fedorov, A. V.; Gardner, D.; Lee, Y. S.; Chu, S.; Valla, T. *Phys. Rev. Lett.* **2012**, *108*, 187001.

(64) Garate, I.; Franz, M. *Phys. Rev. Lett.* **2010**, *104*, 146802.

(65) Nomura, K.; Nagaosa, N. *Phys. Rev. B* **2010**, *82*, 161401.

(66) Wickles, C.; Belzig, W. *Phys. Rev. B* **2012**, *86*, 035151.

(67) Linder, J. *Phys. Rev. B* **2014**, *90*, 041412.

(68) Tserkovnyak, Y.; Pesin, D. A.; Loss, D. *Phys. Rev. B* **2015**, *91*, 041121.

(69) Ferreiros, Y.; Buijnsters, F. J.; Katsnelson, M. I. *Phys. Rev. B* **2015**, *92*, 085416.

(70) Hurst, H. M.; Efimkin, D. K.; Zang, J.; Galitski, V. *Phys. Rev. B* **2015**, *91*, 060401.

(71) Ferreira, G. J.; Loss, D. *Phys. Rev. Lett.* **2013**, *111*, 106802.

(72) Stöhr, J. *J. Magn. Magn. Mater.* **1999**, *200*, 470–497.

(73) van der Laan, G. *J. Phys. Conf. Ser.* **2013**, *430*, 012127.

(74) Sandig, O.; Herrero-Albillos, J.; Römer, F. M.; Friedenberger, N.; Kurde, J.; Noll, T.; Farle, M.; Kronast, F. *J. Electron Spectrosc. Relat. Phenom.* **2012**, *185*, 365–370.

(75) Ohldag, H.; Regan, T.; Stöhr, J.; Scholl, A.; Nolting, F.; Lüning, J.; Stamm, C.; Anders, S.; White, R. *Phys. Rev. Lett.* **2001**, *87*, 247201.

Figures

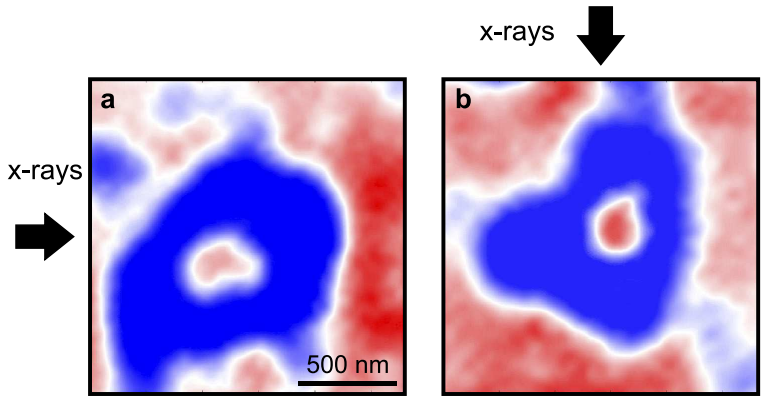

Figure 1: **Isolated skyrmionium — XPEEM observation and contrast simulation.** XPEEM images obtained at the Fe L_3 edge of the NiFe top layer at a temperature of 44 K in zero applied magnetic field. The incoming x-ray directions are indicated: (a) coming from the left and, (b), 90° azimuthally rotated, coming from above. The XMCD contrast has been normalized.

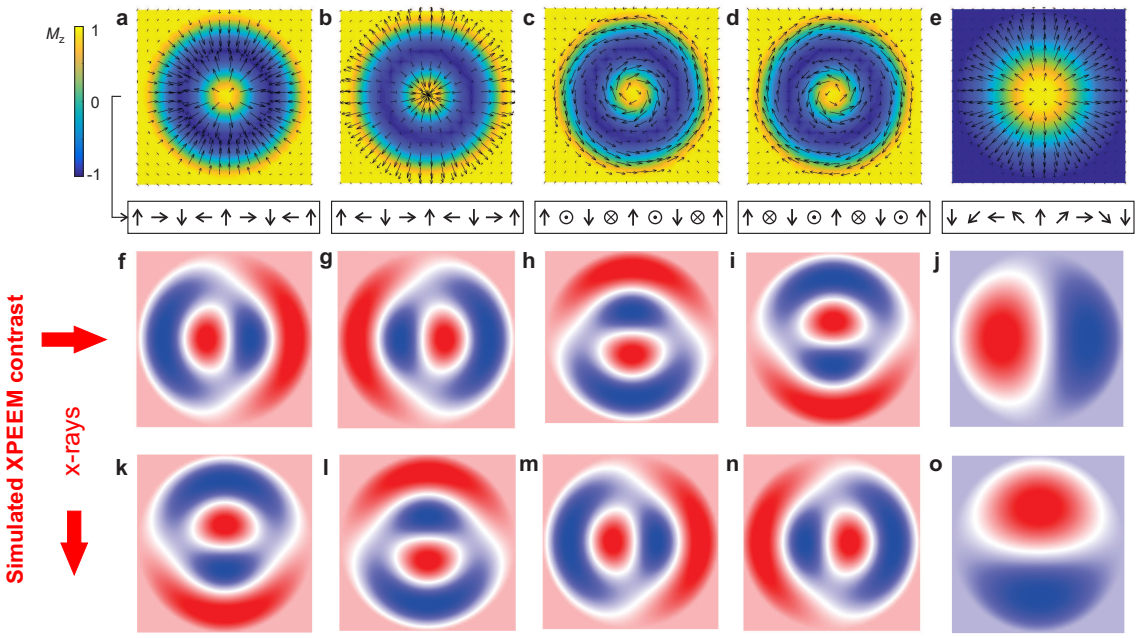

Figure 2: **Spin texture models and their corresponding XPEEM images.** The first row shows possible skyrmionium spin models: (a) (center) diverging Néel-type, (b) converging Néel-type, (c) (center) left-chiral Bloch-type, and (d) right-chiral Bloch-type. Below, cuts through the center show the magnetization in the cross-sectional plane. The middle (f-j) and bottom row (k-o) show the corresponding, simulated XPEEM contrast patterns for the x-rays incident from the left and from above, respectively. Note that the x-ray beam is incident under 16° with respect to the surface normal, i.e., all three magnetization components contribute to the XPEEM image. For comparison, a conventional Néel-type skyrmion is shown in the last column (e,j,o), for which the contrast is distinctly different from any of the skyrmionium configurations.

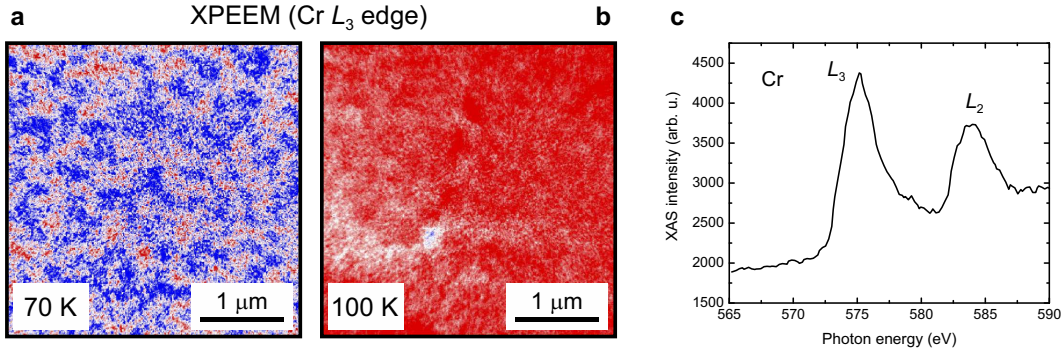

Figure 3: **Magnetic properties of the underlying magnetic topological insulator film.** (a) XPEEM image of the magnetic domain structure in Cr:Sb_2Te_3, with the energy of the x-rays tuned to the Cr L_3 edge. The image was taken at 70 K. The T_C of the film is $\sim$100 K, based on the loss of magnetic contrast seen in (b). Note that the remaining contrast is due to a defect that was used for focusing. (c) XAS of an Cr:Sb_2Te_3 film measured at the $L_{2,3}$ edges of Cr at 70 K in zero applied magnetic field. The XAS lineshape is consistent with nominal Cr valence state of 2+, as expected for substitutional Cr doping on Sb sites. The samples have out-of-plane easy axis anisotropy.[57]

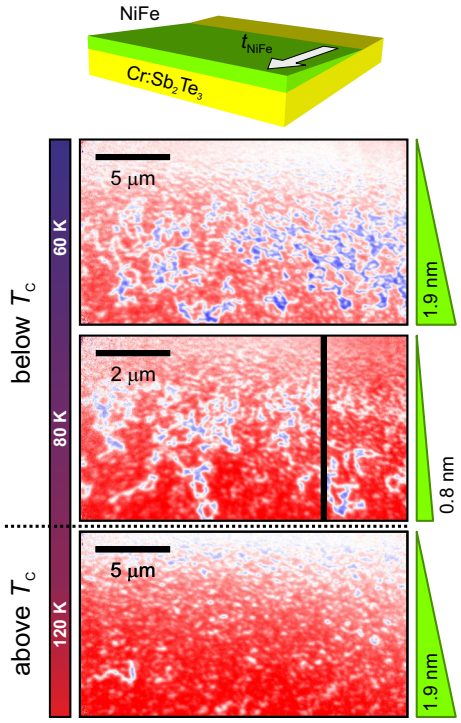

Figure 4: **Temperature-dependence of the XPEEM contrast in the NiFe top layer measured at the Fe L_3 edge in remanence.** Prior to the imaging at the indicated temperature, the sample was subjected to a field of 88 mT. The complex magnetic contrast in the NiFe film vanishes once the sample is heated above the T_C of the magnetic TI film of ∼100 K. The images cover a NiFe film thickness from 0 nm to the indicated values.

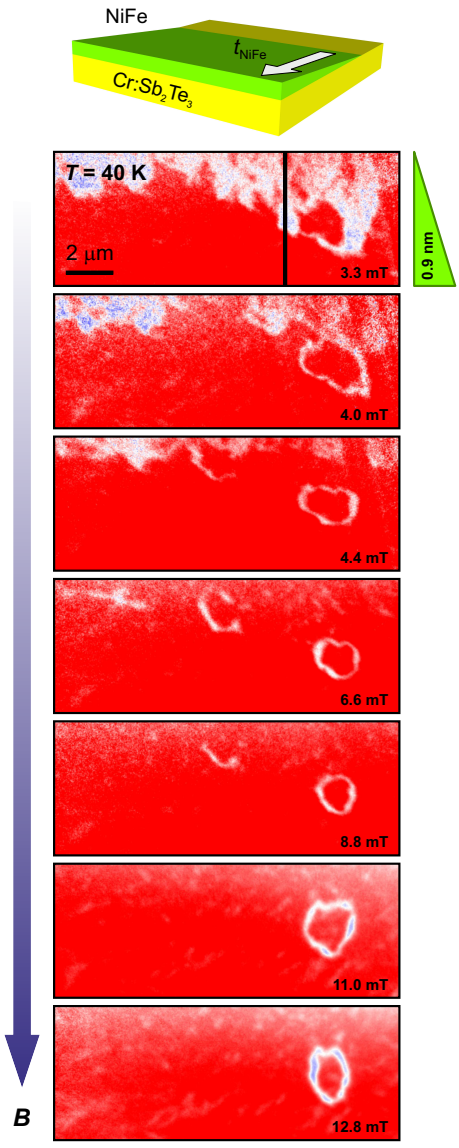

Figure 5: **Field-dependence of the XPEEM contrast in the NiFe top layer, measured at the Fe L_3 edge at a constant temperature of 40 K.** The measurements were taken in a constant applied magnetic field as indicated. With increasing field, the radius of the isolated skyrmionium shrinks. Above 13.2 mT, the skyrmionium vanishes. The images cover a NiFe film thickness from 0 to 0.9 nm.

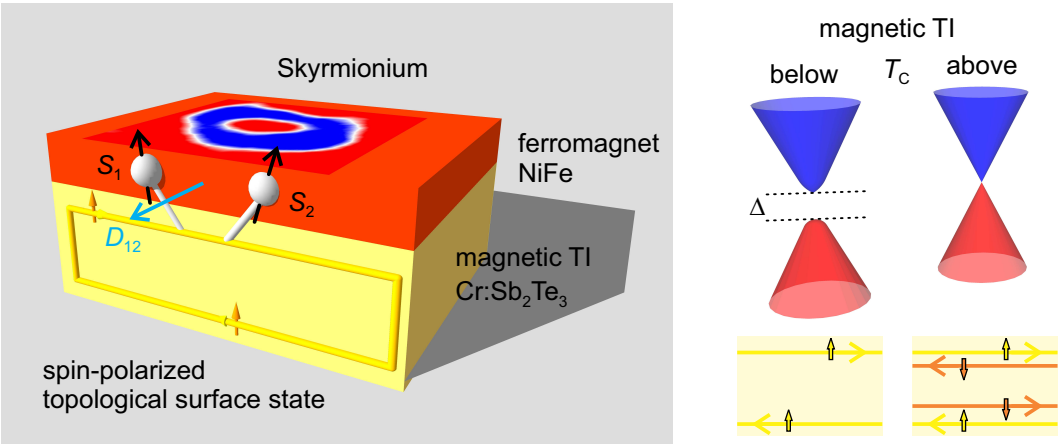

Figure 6: **Illustration of the spin-polarized TSS-mediated DMI interaction leading to the formation skyrmionium in the ferromagnetic NiFe film**. Below the T_C of the magnetic TI, i.e., in the QAH state, a gap appears and the TSS is fully spin-polarized. Above T_C, i.e., in the 'normal' QSH state, there is an equal population of spin-up and spin-down electrons.

For TOC Only

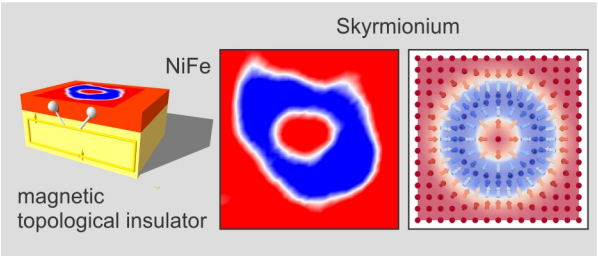

Table of Contents graphic - FOR TOC ONLY